Numerical Investigation of Three-Dimensional Plasma Actuation for Improving Film Cooling Effectiveness

Subrata Roy*
University of Florida, Gainesville, Florida 32611
and
Chin-Cheng Wang†
Yuan Ze University, Taoyuan 32003, Taiwan, Republic of China

DOI: 10.2514/1.T3945

We numerically test a horseshoe plasma actuator for film cooling enhancement on a flat plate. We solve three-dimensional plasma governing equations using the finite element based MIG flow code. The electric force density calculated from the plasma governing equations is then employed as a body force density into a finite volume based Navier–Stokes solver with standard turbulence models for controlling the flow. Such electric force influences attachment of the cold jet to the work surface by actively altering the three-dimensional flowfield in the vicinity of the actuator. We consider two problems related to film cooling. The first problem is to understand the influence of a horseshoe plasma actuator on a flowfield where the cooling jet and the bulk flow speeds are of the same order of the flow induced by plasma itself. The second problem is to validate a previously reported film cooling experiment with a single row of round cooling holes issuing at a 35 deg angle on a flat plate, and then predict any improvement due to plasma actuation. For a unit blowing ratio, the results are compared with the published experimental data and other numerical predictions. The numerical results show a progressive improvement of centerline effectiveness as the electric force density is increased from 0 (no force) to 8 MN/m^3 (maximum). Specifically, an improvement of effectiveness well above 100% is predicted over the standard baseline design for the latest film cooling technology.

Nomenclature

d	=	circular pipe diameter, m
$D_{e,i}$	=	electron or ion diffusion coefficient, m^2/s
E	=	electric field, V/m
e	=	elementary charge, 1.6022×10^{-19} C
F	=	electric force density, N/m^3
k_B	=	Boltzmann's constant, 1.3807×10^{-23} J/K
M	=	blowing ratio
$n_{e,i}$	=	electron or ion density, 1/m^3
p	=	pressure, torr
q	=	separated space charge density, 1/m^3
r	=	recombination rate, m^3/s
T	=	local static temperature, K
V	=	gas velocity, m/s
α	=	Townsend coefficient, 1/m
α_a	=	jet issuing angle
Γ_e	=	electron flux, 1/m^{2}s
ε_0	=	permittivity of free space, 8.8542×10^{-12} F/m
η	=	film cooling effectiveness
$\mu_{e,i}$	=	electron or ion mobility, m^2/sV
ρ	=	gas density, kg/m^3
ϕ	=	potential, V

Subscripts

e	=	electron
fs	=	freestream
i	=	ion
j	=	cooling jet
s	=	work surface

Presented as Paper 2010-1092 at the 48th AIAA Aerospace Sciences Meeting Including the New Horizons Forum and Aerospace Exposition, Orlando, FL, 4–7 January 2010; received 1 May 2012; revision received 29 January 2013; accepted for publication 28 February 2013; published online 4 June 2013.

*Associate Professor, Mechanical and Aerospace Engineering. Associate Fellow AIAA.

†Assistant Professor, Mechanical Engineering, 135, Yuan-Tung Rd. Chung-Li; ccwang@saturn.yzu.edu.tw. Member AIAA.

I. Introduction

CROSSFLOW jets have been widely successful in many engineering problems including the film cooling of gas turbine blades. These blades suffer from very high thermal stresses due to hot effluent gases from the combustion chamber. The problem worsens with increasing turbine inlet temperature used for higher thermal efficiency. Repetitive thermal stress over a long duration significantly affects the lifetime of turbine blades. There are several methods of cooling turbine blades for increasing their lifetime. Film cooling is one of the most promising of such methods, where cold jets are injected through rows of surface holes located in the spanwise direction on the blade. These jets penetrate into the hot freestream gas forming a three-dimensional (3-D) bound vortical structure that promotes attachment of a thin film of cold gas over the blade surface, protecting it from thermal stress. In traditional designs, the attachment of the cold jet to the blade surface becomes aggressively difficult as the momentum ratio of the injected air to the crossflow (i.e., the blowing ratio M) increases, causing a local lift off of the cold film just downstream of the cooling hole. Haven and Kurosaka [1] examined the effect of the hole exit geometry on near field characteristics of crossflow jets in a canonical fashion. From the experimental observation shown in Fig. 1, we can see the liftoff behavior of the kidney vortices as the cold jet interacts with the hot freestream gas.

Numerous numerical studies have been performed for improving cooling effectiveness by reducing liftoff effect. Roy [2] showed that lowering the issuing angle maximizes the cooling efficiency. Walters and Leylek [3] provided an understanding of the flow physics for different film hole lengths, diameter ratios, and blowing ratios using cylindrical cooling holes. Hyams and Leylek [4], Azzi and Jubran [5], and Zhang and Hassan [6] presented different shaped holes for detailed analysis of film-cooling physics. The results indicated that changes in film-cooling hole shape could strongly affect the downstream behavior of the film. Na and Shih [7] proposed a ramp modification upstream of the holes to modify the interaction of

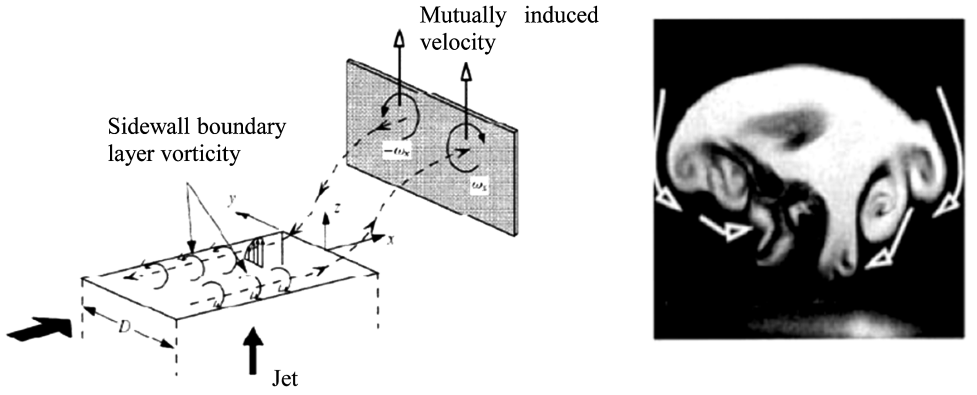

Fig. 1 Schematics show a) kidney vortices due to the hole sidewall vorticity and b) kidney vortices at downstream of the coolant hole with elliptic hole geometry [1].

incoming flow and cooling jet. Their results showed that a ramp design gave two times higher laterally averaged effectiveness than without a ramp.

For more accurate numerical simulation, Garg [8] and Heidmann et al. [9] considered realistic film-cooled turbine vane geometry including the plenum and hole pipes with Wilcox's κ-ω turbulence model [10]. These studies provide good details of the flow. However, the spanwise vortices are complex to resolve using κ-ω turbulence model. The two competing factors limiting any turbulence models efficacy in capturing these processes are computational accuracy and efficiency (i.e., CPU cost). Researchers used large-eddy simulation (LES) and direct numerical simulation (DNS) to capture small and large scale flow details. Zhong and Brown [11] conducted DNS for solving a 3-D film cooling problem with multiple holes. They computed cooling effectiveness that showed good agreement with experimental results for low blowing ratio cases of $M = 0.25$ and $M = 0.43$. However, both DNS and LES are computationally limited for high Reynolds number flows. As a remedy, a detached eddy simulation (DES) turbulence model is widely used for capturing reasonable description of the dynamic flow structures at higher Reynolds numbers. For example, Kapadia et al. [12], Martini et al. [13], and Kim and Hassan [14] performed DES of film-cooling flows. Their results indicate that the mixing process downstream of the hole is highly anisotropic due to a much stronger turbulent diffusion process in the transverse direction.

Several experimental efforts [15–17] have been also documented in the literature. Sinha et al. [15] provided detailed experimental data for film cooling effectiveness with different density ratios and blowing ratios on a flat plate with a row of inclined holes. The results showed that the centerline effectiveness scaled with the mass flux ratio and that the laterally averaged effectiveness depended on density ratio and momentum flux. Bell et al. [16] studied five different shaped holes for different blowing ratios, momentum flux ratios, and density ratios. Some of these designs increase lateral spreading of the cold jet. Bunker [17] also provided a review of the shaped holes for film cooling. He summarized that shaped holes had higher centerline and spanwise effectiveness than round holes and concluded that for shaped holes the cooling effectiveness showed little variation over a range of blowing ratio ($0.5 \leq M \leq 2$). Ekkad et al. [18] investigated cooling effectiveness for different blowing ratios ($0.25 \leq M \leq 2$) for a range of jet pulsing frequencies between 5 and 20 Hz, and duty cycle levels between 10 and 100%. Results indicate the higher effectiveness and lower heat transfer coefficients are obtained at the reduced duty cycles. Bogard and Thole [19] provided a thorough review of the literature on physical descriptions and various influences on film cooling performance. It was found that there are strong influences of freestream turbulence, surface curvature, and hole shape on the performance of film cooling.

The complex dynamic nature of a film-cooling flow makes it a candidate for active control using a dynamic force that varies temporally and spatially working with the dominant turbulence scales. Reported experimental and numerical results show that dielectric barrier discharge (DBD) actuators are effective in controlling the flow [20,21]. Surface compliance, rapid response, lack of moving parts, and easy installation are a few advantages of plasma actuators. Specifically, due to the lack of mechanical components, the lifetime of the actuator could be significantly extended as compared to other mechanical/electromechanical devices such as synthetic jet actuators. We proposed a concept using plasma electric force to actively enhance interaction of cool air jets with hot crossflow for improved cooling of hot surfaces [22,23]. The hot freestream gas will enhance dissociation and hence, help plasma generation due to ionization in the vicinity of the electrodes. Both pulsed dc- and ac-powered plasma actuators can induce such active control over the dynamics of film cooling. A novel aspect of these actuators is that one may vary the spatial and temporal scales over which the energy is added. The momentum transfer between the plasma and gas happens due to collisional momentum transfer between charged ions and neutral atoms. Such actuation of the flow is active and near instantaneous, does not require any mechanical parts, and the actuator electrode sets can be applied as a patch on the surface of the existing ceramic coating of the turbine blade or embedded into the coating. There could be practical considerations like surface oxidation of the electrodes and spallation. In our prior study, we employed a phenomenological electric force model along a horseshoe geometry for the 3-D flow simulation [23]. Here, we solve the fully 3-D governing equations for the plasma and flow simulation. The 3-D electric force density is calculated from the electric field and the space charge separated plasma density. Assuming that the plasma timescales are orders of magnitude smaller than the flow timescale, we use the time average of the electric force distribution as a body force in the Navier–Stokes equations.

II. Problem Description

We employ a horseshoe-shaped plasma actuator with two asymmetrically displaced curved electrodes separated by a dielectric (insulating) material. One of the electrodes is exposed to the air and the other one is encapsulated within the dielectric material. The neighboring gas ionizes over the exposed surface due to an applied electric field between these two electrodes that are powered with a sinusoidal voltage difference at a kHz frequency. The discharge is driven by a high electric field ($\sim 10^6$ V/m) that triggers electron emission from the instantaneous cathode. These electrons collide with neutral molecules of the working gas initiating ionization, and resulting in a separated space charge. As a product of this electric field and the space charge, an electrohydrodynamic (EHD) body force is induced. Interestingly, irrespective of the polarity of the electrodes, the majority of the EHD force is directed from the exposed electrode to the grounded electrode [24].

Starting from plasma principles, we study two separate problems to understand the effect of plasma actuation on a film-cooling flow. Problem I is the thermal stress management for a very low speed

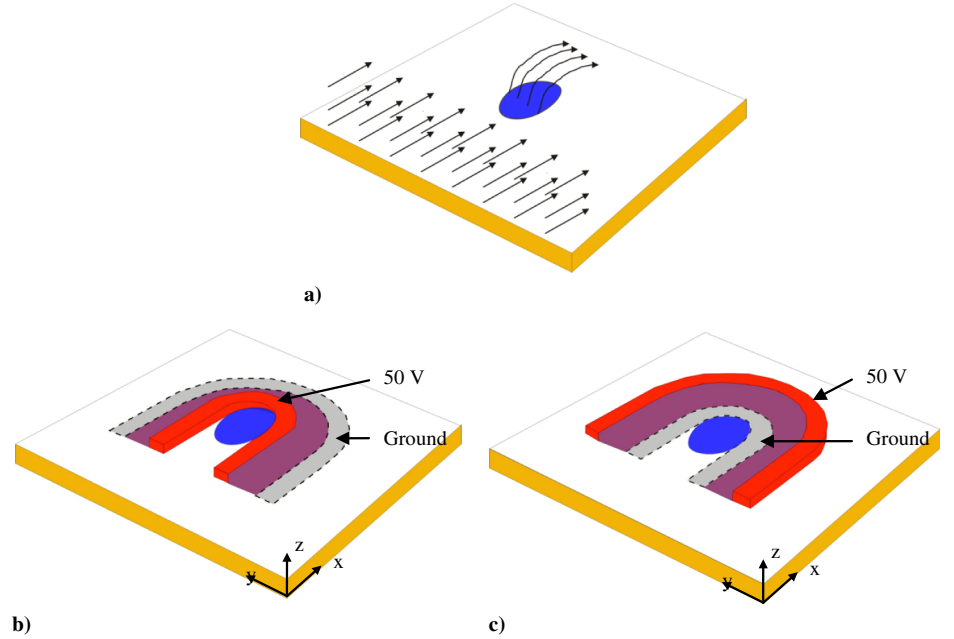

Fig. 2 Schematics show the a film-cooling flow for a) the baseline case, b) the case of an outward plasma force, and c) the case of an inward plasma force.

(laminar) hot gas flow over a flat plate. We consider two different powering schemes to generate plasma forces as shown in Fig. 2 and compare them with film cooling in the absence of plasma forces. The baseline case with no plasma effect is shown in Fig. 2a and horseshoe plasma actuators with different setups are shown in Figs. 2b and 2c. For all cases in problem I, the hot freestream gas comes from the x direction with uniform velocity of 0.3 m/s and temperature of 300 K. The cold jet comes from a coolant hole and injects into the bulk region with an angle of 45 deg, velocity of 0.42 m/s, and temperature of 150 K. To reduce high enthalpy related issues, the temperatures of the freestream gas and the coolant jet are chosen based on [15]. All boundary conditions are shown in Fig. 3. We impose velocity inlet conditions at $x = 0$ and $x = 0.0003$ m and a zero pressure outlet condition at $x = 0.0006$ m. Symmetry boundaries are maintained at $y = 0$ and 0.0006 m. At the bottom wall, an adiabatic no-slip wall boundary condition is imposed. The flow actuation is done by a set of horseshoe-shaped electrode pairs between which electric potential generates an electric body force that is dominant inside the viscous boundary layer. We apply a voltage $\phi > 0$ to the inner electrode and ground the outer electrode to create an outward electric force from the horseshoe actuator. Contrarily, the outer electrode is powered and the inner electrode is grounded for generating an inward directed plasma force. The latter arrangement will generate a force that will reduce the jet momentum coming out of the coolant hole. Note that these electrodes are separated by a thin 0.00002 m dielectric barrier of Kapton between them. The plasma actuation is directly linked with a near-instantaneous Lorenzian momentum coupling between the gas and the charged particles. Figure 3 shows the top view and the side view of the computational domain for the first problem.

Problem II is film cooling with a realistic velocity ratio (i.e., V_j/V_{fs}) of 0.5. We compare our numerical results with Sinha et al.'s experiment [15] for validation purposes. Figure 4 describes the control volume of freestream air passing over a flat (blade) surface that is an adiabatic wall with an inward directed plasma force near the coolant hole. This flat surface has a row of injection holes through which the cool air is issued at an angle $\alpha_a = 35$ deg. The cool jet at temperature $T_j = 150$ K is injected into the hot freestream of $T_{fs} = 300$ K. The injection ducts are circular pipes with diameter equal to $d = 0.00254$ m. The injection hole formed by the intersection of the injection pipe with the wind tunnel is an ellipse with the minor and the major axes d and $D = d/(\sin \alpha_a)$,

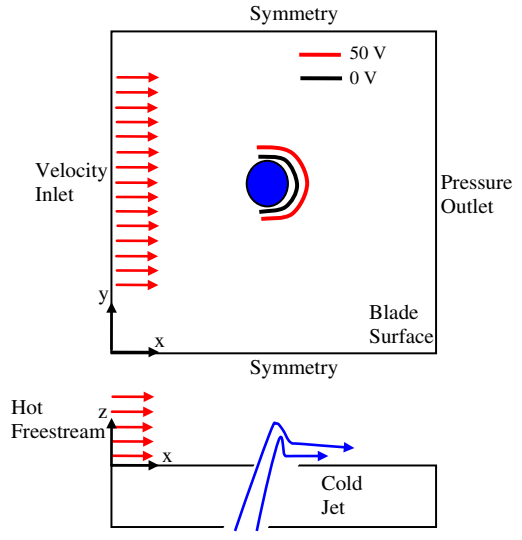

Fig. 3 Schematics show the top view and the side view of an inward arrangement of computational domain.

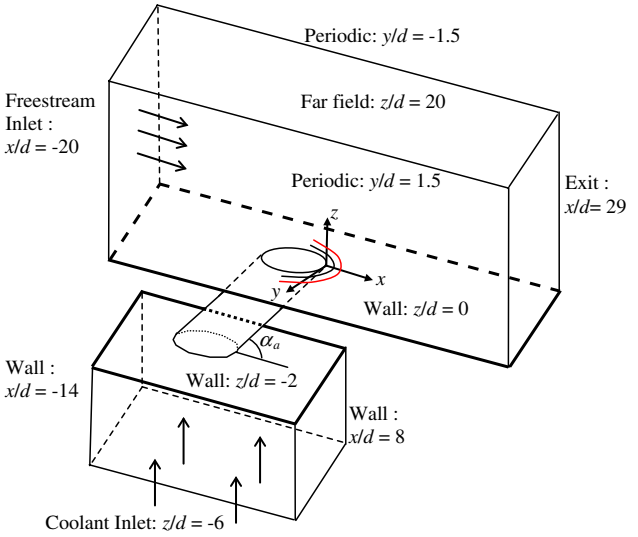

Fig. 4 Schematic shows the geometry and boundary conditions are based on reported test setup [15].

respectively. The distance between the hole centers is $L = 3d$. The selected mean flow velocities, static pressures, and temperatures (i.e., densities) in the injection pipe and the wind tunnel gives a blowing ratio $M = 1$. The freestream inlet section is located at $x = -20d$ and the exit is located at $x = 29d$. The mass flow rate maintained at the freestream inlet is 0.05372 kg/s, whereas that for the coolant inlet is 0.003 kg/s with a density ratio of $\rho_j/\rho_{fs} = 2$ and a velocity ratio of $V_j/V_{fs} = 0.5$. The exit is maintained at zero gauge pressure. The domain extends from the plenum base at $z = -6d$ to $z = 20d$ where a pressure-far-field boundary condition is applied. The periodic boundary condition is applied in the crosswise direction (at $y = \pm 1.5d$) in the computational domain. For the coolant plenum, a no-slip wall condition is applied at $x/d = -14$ and $+8$, and $z/d = -2$ surfaces. The mass flow inlet condition that would ensure a blowing ratio of unity is assumed at $z/d = -6$. Other dimensions and boundary conditions are shown in Fig. 4. For standard DBD actuators, the electric force density is measured to be $\sim$kN/m^3, which consumes tens of W of power [24]. However, such small electric force density may not be useful to control the flow over the actual turbine blade. The electric force density has to be three orders of magnitude higher than the standard RF plasma actuator. Even such higher force density ($\sim$MN/m^3) will only use a small fraction of power (less than 1% of the turbine power) for such an arrangement, which may eventually reduce the energy budget by more effective cooling.

Two important parameters for comparing film cooling performance are the effectiveness η and the blowing ratio M. The effectiveness is defined as $\eta = (T_{fs} - T_s)/(T_{fs} - T_j)$, where T_s, T_j, and T_{fs} are the work surface, cooling jet, and freestream gas temperatures, respectively. The blowing ratio is the momentum ratio of the jet over the freestream $M = \rho_j V_j/\rho_{fs} V_{fs} = 1$, based on the work of Sinha et al. [15]. The density ρ_j and velocity V_j of the fluid at the jet exit plane are related to the freestream density ρ_{fs} and velocity V_{fs} such that $\rho_j/\rho_{fs} = MV_{fs}/V_j$. The turbulence intensity is defined as $I = u'/U$, where u' is the rms of the turbulent velocity fluctuations and U is the mean velocity. Here, $I = 0.05$ is maintained based on the calculated turbulent kinetic energy.

III. Numerical Model

We employ a hydrodynamic model for multiscale dielectric barrier discharge simulation at atmospheric pressures. The model uses an efficient finite element algorithm. The unsteady transport for electrons and ions is derived from fluid dynamics in the form of mass conservation equations. The species momentum is modeled using the drift–diffusion formulation under local thermal equilibrium approximation that can be derived from the hydrodynamic equation [25]. The continuity equations for ion and electron number densities and Poisson's equation are given by

$$\frac{\partial n_i}{\partial t} + \nabla \cdot (n_i \mathbf{V}_i) = \alpha|\Gamma_e| - r n_i n_e$$
$$\frac{\partial n_e}{\partial t} + \nabla \cdot (n_e \mathbf{V}_e) = \alpha|\Gamma_e| - r n_i n_e$$
$$|\Gamma_e| = \sqrt{(n_e V_e)_x^2 + (n_e V_e)_y^2 + (n_e V_e)_z^2} \tag{1}$$

$$n_i \mathbf{V}_i = n_i \mu_i \mathbf{E} - D_i \nabla n_i \quad n_e \mathbf{V}_e = -n_e \mu_e \mathbf{E} - D_e \nabla n_e \tag{2}$$

$$\nabla \cdot (\varepsilon \mathbf{E}) = e(n_i - n_e) = eq \tag{3}$$

where n_e and n_i are number densities of electron and ion, respectively, q is the separated space charge density, $\mathbf{V}(V_x, V_y, V_z)$ is the species hydrodynamic velocity, and the electric field $\mathbf{E}$ (E_x, E_y, E_z) is given by $\mathbf{E} = -\nabla\varphi$ (i.e., the gradient of electric potential φ). In Eqs. (1–3), $r \sim 2 \times 10^{-13}$ m^3/s is the electron-ion recombination rate, ε is the dielectric constant, and subscripts i and e denote positive ion and electron, respectively. The discharge is maintained using a Townsend ionization scheme. The ionization rate is expressed as a function of electron drift velocity $|\Gamma_e|$ and Townsend coefficient α:

$$\alpha = Ap \exp(-B(|\mathbf{E}|/p)) \tag{4}$$

where A and B are preexponential and exponential constants, respectively, and p is the pressure. The system of Eqs. (1–3) is normalized using the following normalization scheme: $\tau = t/t_0$, $z_i = x_i/d$, $N_e = n_e/n_0$, $N_i = n_i/n_0$, $u_e = V_e/V_B$, $u_i = V_i/V_B$, $\phi = e\varphi/k_B T_e$ where k_B is Boltzmann's constant, $V_B = \sqrt{k_B T_e/m_i}$ is the Bohm velocity, reference length d is usually a domain characteristic length in the geometry, the reference time is $t_0 = 10^{-8}$ s, and the reference density is $n_0 = 10^{15}$ m^{-3}. The ion mobility and diffusion at 300 K, as well as electron mobility and diffusion at 11,600 K (i.e., 1 eV), are given by Surzhikov and Shang [26]. We do not apply an external magnetic field, and the induced magnetic field is negligible. Finally, the following equations are solved:

$$\frac{\partial n_i}{\partial t} + \frac{\partial}{\partial x}\left\{n_i\mu_i E_x - D_i\frac{\partial n_i}{\partial x}\right\} + \frac{\partial}{\partial y}\left\{n_i\mu_i E_y - D_i\frac{\partial n_i}{\partial y}\right\} + \frac{\partial}{\partial z}\left\{n_i\mu_i E_z - D_i\frac{\partial n_i}{\partial z}\right\} = \alpha|\Gamma_e| - r n_i n_e$$
$$\frac{\partial n_e}{\partial t} + \frac{\partial}{\partial x}\left\{-n_e\mu_e E_x - D_e\frac{\partial n_e}{\partial x}\right\} + \frac{\partial}{\partial y}\left\{-n_e\mu_e E_y - D_e\frac{\partial n_e}{\partial y}\right\} + \frac{\partial}{\partial z}\left\{-n_e\mu_e E_z - D_e\frac{\partial n_e}{\partial z}\right\} = \alpha|\Gamma_e| - r n_i n_e \tag{5}$$

where $\mu_i = 1.45 \times 10^{-1}/p$ (m^2/sV) is the ion mobility, $\mu_e = 4.4 \times 10/p$ (m^2/sV) is the electron mobility, D_i and D_e are the ion and electron diffusion coefficients, respectively, calculated from the Einstein relation that is a function of ion and electron mobility as well as ion and electron temperature, i.e., $D_i = \mu_i T_i$ and $D_e = \mu_e T_e$. For an electric potential of 10^6 V/m under atmospheric pressure with a bulk gas density of 2.48×10^{25} m^{-3}, the reduced electric field is approximately equal to 40 Td. Based on the solution of Boltzmann equation [27] at this condition, the electron mobility is equal to 0.05835 m^2/Vs, which is within 1% of the value (0.05789 m^2/Vs) calculated using the approximate equation given in [26]. The following boundary conditions are enforced for the plasma simulation. At the exposed electrode, the electronic flux is based on the electron thermal velocity and is directed toward the electrode. The positive ion flux normal to the exposed electrode is considered to be zero if the electric field is directed away from the electrode. The initial ion and electron number densities are assumed to be uniform and equal to 10^{15} m^{-3} in the plasma domain, whereas these charged particle densities are set to zero within the dielectric material. Based on a sheath analysis reported for a similar problem [25], the smallest mesh size is kept at 10^{-5} m, which is enough to capture the relevant physics within the sheath thickness under this condition. A fixed time step of 10^{-11} s (of the order of dielectric relaxation time) is employed for solving plasma equations.

We apply time average of the electric force density ($\mathbf{F} = e\mathbf{E}q$) calculated from Eqs. (3–5) in the Navier–Stokes equations as a body force for an incompressible Newtonian fluid shown next:

$$\nabla \cdot \mathbf{V} = 0 \quad \rho\frac{D\mathbf{V}}{Dt} = -\nabla p + \mathbf{F} + \mu\nabla^2\mathbf{V} \quad \rho c_p\frac{DT}{Dt} = k_H\nabla^2 T + \Phi \tag{6}$$

where ρ is the fluid density, $\mathbf{V}$ is the fluid velocity vector, μ is the fluid viscosity, k_H is the fluid conductivity, T is the fluid temperature, and Φ denotes the viscous dissipation.

Equations (5) and (6) are discretised using a finite element method (FEM) based module driven 3-D MIG (multiscale ionized gas) flow code. The in-house MIG flow code has been verified and used for many applications such as plasma governing equations and Navier–Stokes equations. Computed solutions show details of the distribution of charged and neutral particles and their effects on the flow dynamics [22,23,25]. The forward temporal evolution is evaluated using the fully

implicit time stepping procedure. The Newton–Raphson scheme is used for dealing with nonlinear terms. To solve the sparse matrix, we employ the iterative GMRES (generalized minimal residual) solver. The assembly procedure involves storing only the nonzero elements of the Jacobian matrix in the form of a linear array, and the corresponding row and column locations are stored using an incremental flag. The solution is assumed to have converged when the L_2 norms of all the normalized solution variables and residuals are below a chosen convergence criterion of 10^{-3}.

For problem II, the 3-D fluid model is solved by a commercial CFD package, ANSYS Fluent. According to Sinha et al.'s experiment [15], a compressible and steady turbulent flow is assumed. For Sinha et al.'s experiment [15], the Reynolds number based on the hole diameter and inlet conditions was 16,100. Our numerical simulation maintains geometric and kinematic similarity with the experiment in [15] by matching the same Reynolds number ($Re = 16100$) and blowing ratio ($M = 1$). This resulted in scaling down the experimental geometry of [15] by a factor of five to a hole diameter of 0.00254 m for our numerical simulation. This allows for less computational mesh and faster solution convergence. The maximum Mach number achieved in the flowfield is below 0.3. We employ the density-based formulation of the computer code while minimizing compressibility effects. We interpolate the time-averaged electric force density as a source term in the gas flow momentum equations using the UDF (user defined functions). We use the ideal gas approximation and the AUSM (advection upstream splitting method) solver closed with RNG (renormalized group) κ-ε turbulence model with standard wall function. In a previous publication, we modeled turbulence for the baseline case using detached eddy simulation (DES) [12]. These reported results, albeit expensive, were much closer to the experimental data. Here, to reduce computational cost, we use κ-ε turbulence model, which is suitable for the steady-state flow assumption. The Courant number is set equal to unity for solution control. A second-order upwind discretization method is employed. The solution convergence is determined when the residual among the continuity, momentum, energy, turbulent kinetic energy, and turbulent dissipation are less than 10^{-3}. For problem I, both plasma and fluid simulations are carried out under the same mesh size of 92,160 elements. For the simulation, the time step is 10^{-11} s and the grid size is 10^{-5} m, which is sufficiently resolved to capture relevant sheath physics and definitely well resolved for the flow physics. The simulation is considered converged when residuals for electron and ion number densities and the electric potential are below 10^{-3}. For problem II, it is well known that a coarse grid cannot resolve the effect of the downstream vortices. Problem II is assumed to have steady flow condition. The simulation is converged when the residuals are below 10^{-3}. The computational mesh of 200,000 cells is chosen based on the grid independent study [28] for better convergence and less computational cost. We used previous grid resolution studies for problem II only because the fluid thermal interaction for the film cooling problem is a more involved problem. For problem I, the computational domain was sufficient to capture the sheath physics and fluid physics. All cases for problem II require approximately 1400 iterations for convergence.

IV. Results and Discussion

Two problems are investigated in this paper. As mentioned earlier, problem I focuses on understanding the basic influence of a horseshoe actuator on the surrounding flow under a near-quiescent condition (with a freestream velocity of 0.3 m/s). For problem II, the baseline case is compared with Sinha et al.'s experimental data [15] and two other numerical works [29,30]. Other cases are scaled with different levels of plasma force density for improving film cooling effectiveness. Because we use an inherently time-averaged turbulence model for problem II, the computed results are presented at the steady state. For a blowing ratio $M = 1$, the interaction of flow profiles between the wind tunnel and cold jet inlet is very complex. This is due to the fact that for the range of velocities the boundary layers are not thin everywhere within the pipe. For very thick boundary layers, the flow close to the wall behaves like a typical boundary layer, whereas for a very thin boundary layer a wall-jet structure forms downstream of the jet exit. Such flow motion creates a bound kidney-shaped vortical structure that stretches downstream along the primary flow direction.

A. Problem I

The temperature distribution of the baseline case is shown in Fig. 5. The results show how the hot freestream of 300 K interacts with the cold jet of 150 K at $(x, y, z) = (0.0003, 0.0003, 0.0)$ m. This range of temperature is based on the experiment [15]. The attachment of the cold fluid protects the downstream surface from high thermal stresses due to high temperature. We can roughly define a region where the surface temperature is less than 230 K. For the case of an outward plasma force shown in Fig. 6, we impose a dc potential of 50 V to the exposed (previously called inner) electrode on the dielectric surface and ground the (previously called outer) electrode inside the dielectric. The gap between the electrodes is equal to 0.00004 m. This type of dc microplasma has been tested by Wilson et al. [31,32]. Such microplasmas have evolved into plasma-enhanced chemical vapor deposition for microelectromechanical system and integrated circuit processing. Figure 6a shows the electric force vectors overlaid on the flooded contours of charge separation (at the xz plane, $y = 0.0003$ m) and potential distribution (at the xy plane, $z = 0.00003$ m). The force is acting outward from powered electrode to the grounded electrode in three dimensions. The peak of charge separation is $\sim 10^{15}$ m^{-3}. The potential varies from 50 to 0 V between the exposed and the grounded electrode. The force density for this electrode arrangement (not shown) is in the order of kN/m^3. We can see such force actuation drastically changes the flow path of the cold jet upward as shown in Fig. 6b. From the top view of the work surface at $z = 0.00003$ m, the temperature is above 290 K at downstream of the coolant hole. To induce an inward plasma force, we apply potential to the outer electrode on the work surface as shown in Fig. 7a. This reduces the cold jet momentum as shown in Fig. 7b. Here, the average temperature at locations downstream of the coolant hole is much lower than the baseline case. Hence, the film cooling effectiveness has been greatly improved. From previous tests, we can see the case with an inward plasma force is useful for attaching the cold jet to the work surface and increasing film cooling effectiveness

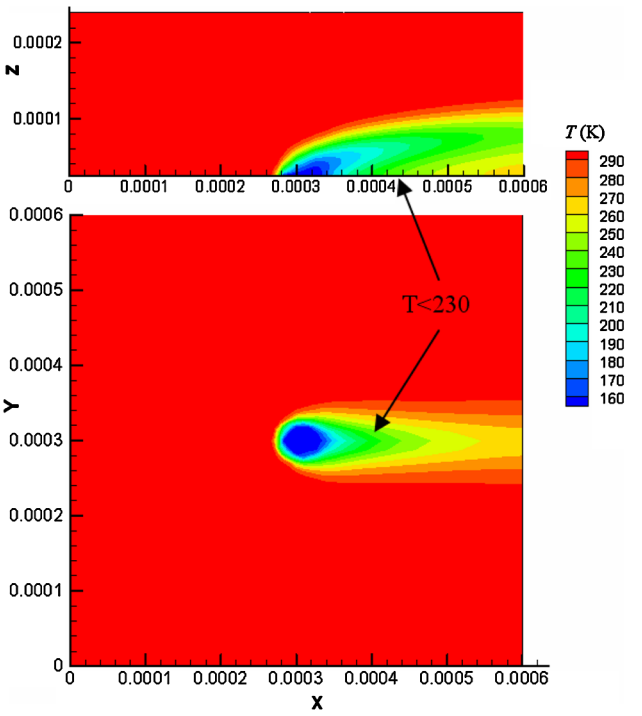

Fig. 5 Temperature distribution on the xz plane of $y = 0.0003$ m and on the xy plane of $z = 0.00003$ m for the baseline case without plasma force.

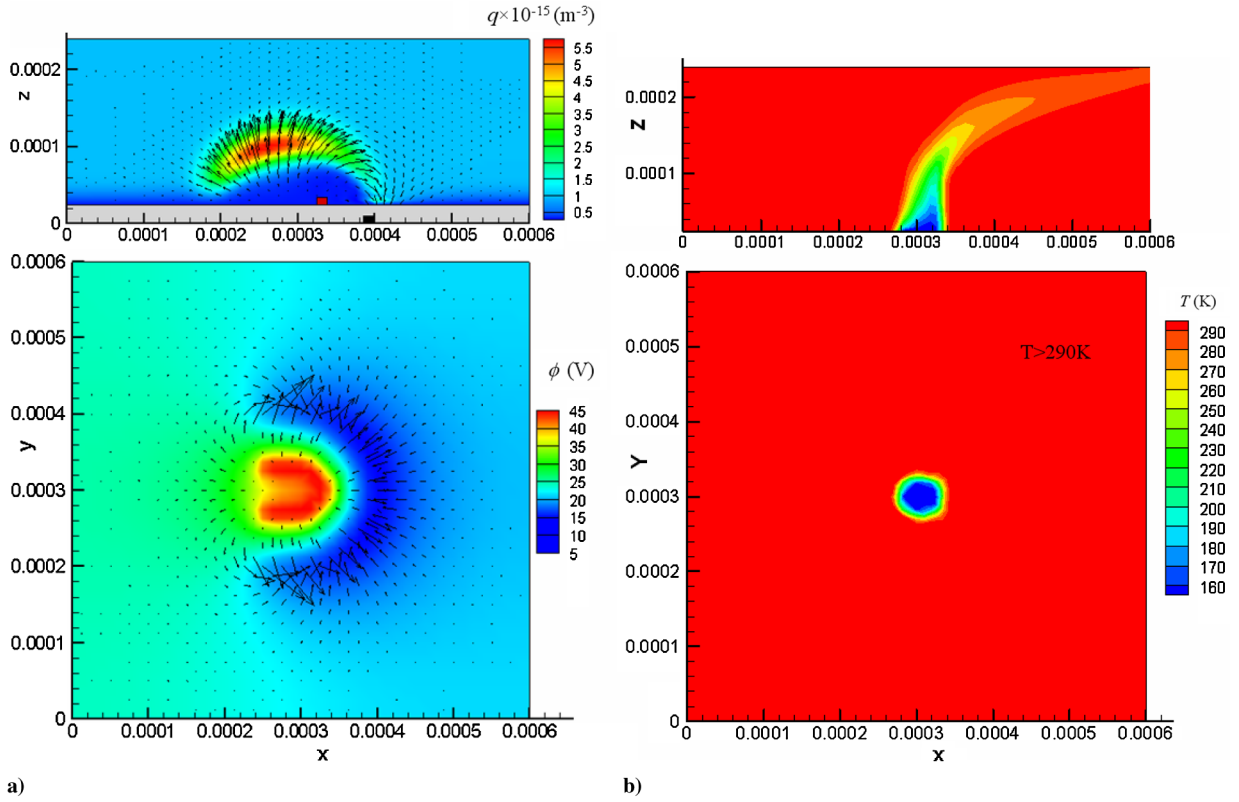

Fig. 6 For an outward plasma force, a) the charge q, the potential ϕ and b) the resulting temperature T are plotted.

on both streamwise and spanwise directions. We explore this further for the film cooling problem II with a realistic blowing ratio.

B. Problem II

Here, we investigate the interaction of a cold jet of 150 K issuing at an angle of 35 deg into a freestream gas at 110 m/s and 300 K, and its influence on the temperature distribution of the plate. To maintain a blowing ratio of unity, the flow speed at the intersection of the injection duct and the flat plate ranges between 50 to 100 m/s. At the location of $x = -3d$, the local Reynolds number (Re_x) of 320,152 is calculated based on the freestream velocity. Corresponding disturbance thickness is equal to $\delta_x = 5 * 17d/(Re_x)^{0.5} =$

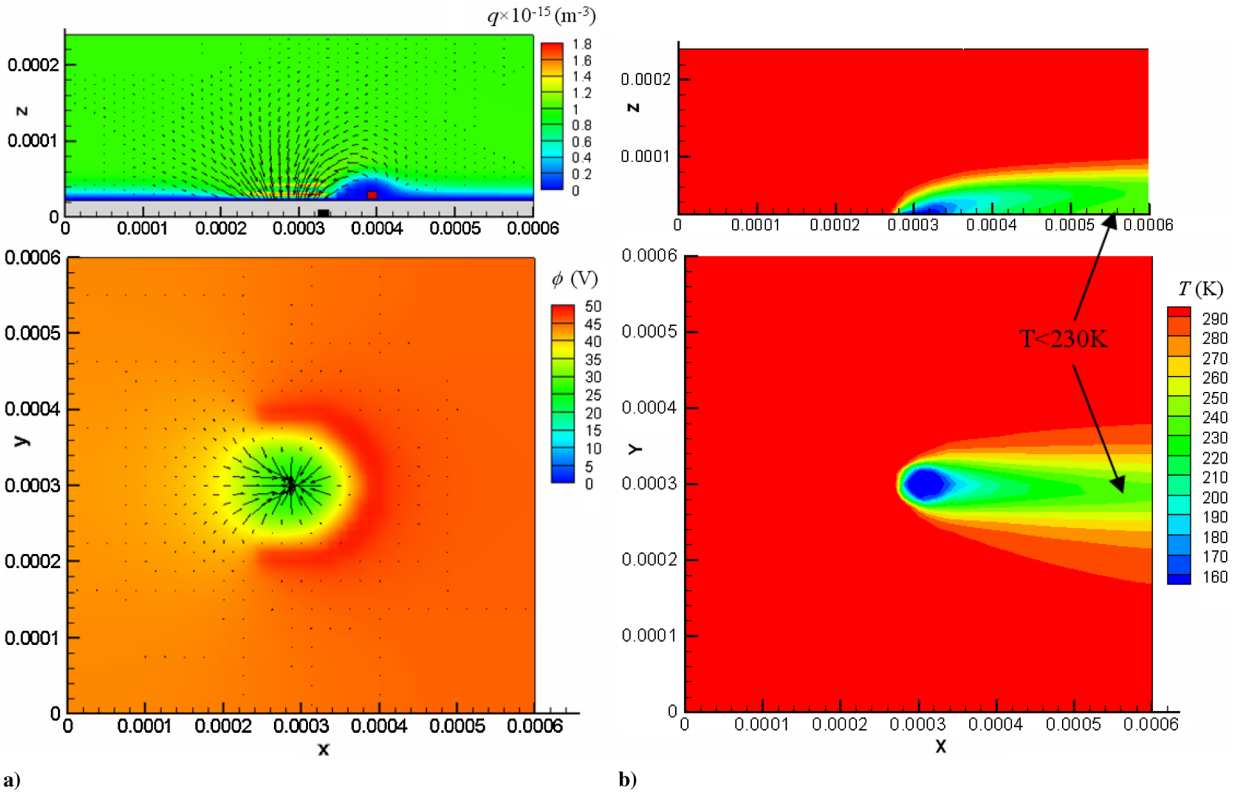

Fig. 7 For an inward plasma force, a) the charge q, the potential ϕ and b) the resulting temperature T are plotted.

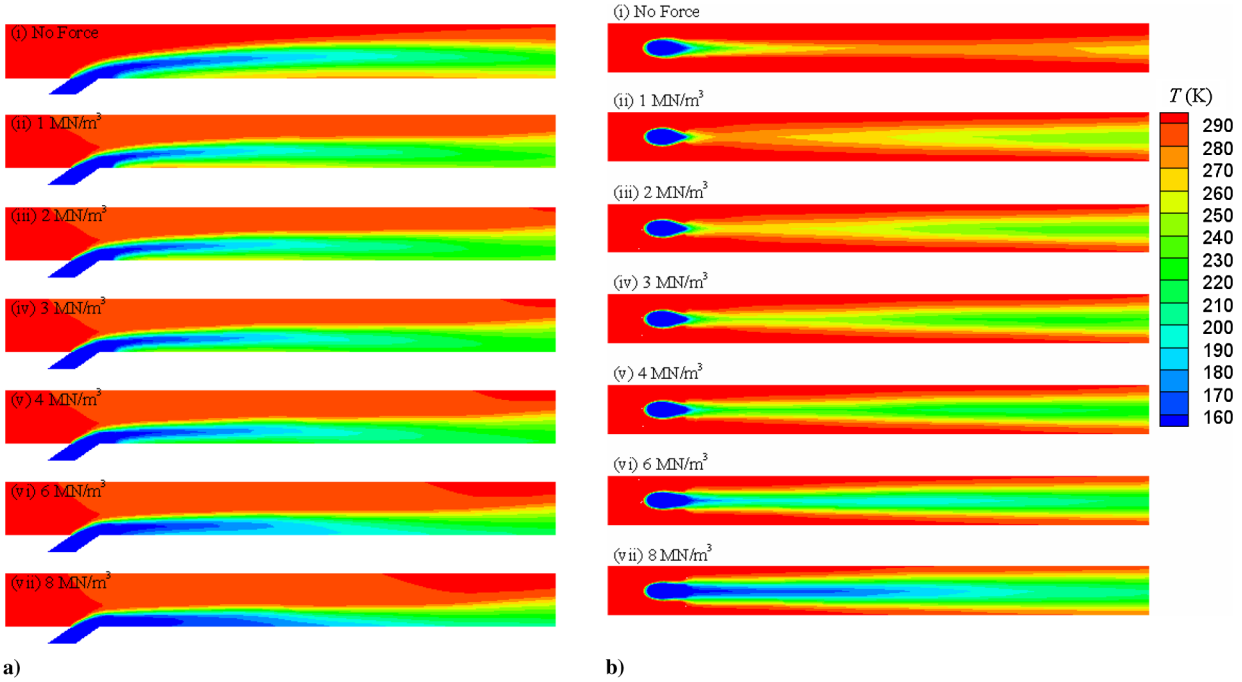

Fig. 8 Temperature contour with different force density for the plane at a) $y = 0$ and b) $z = 0$.

0.00038 m, the momentum thickness is equal to $\theta_x = 0.133\delta_x = 0.00005$ m, and the momentum-thickness Reynolds number is $Re_\theta = 376$. At $x = -d$ (upstream of the hole), $Re_\theta = 1027$. For effectively controlling such a high momentum flow, we need to scale the plasma force density from kN/m^3 to MN/m^3. We have demonstrated the feasibility of similar force density scaling in a recent publication on microscale plasma actuators [33]. It is important to note that the curved actuators employed here generate fully 3-D vortices [34–36] with a large range of frequencies making them particularly suitable for actuating the hairpin structures within a turbulent flow. Figure 8a plots the temperature distribution on the vertical midplane ($y = 0$), whereas Fig. 8b shows the temperature distribution on the horizontal work surface ($z = 0$). Altogether, seven film cooling cases are simulated with force density varied from an initial zero (no force) to a maximum of 8 MN/m^3. It is obvious that the liftoff effect causes a significant reduction in film cooling effectiveness for the baseline case shown in Fig. 8a and 8b where the force density (i) No force. As we increase the force density, the flow completely attaches to the work surface. Importantly, such actuation applied in a 3-D manner demonstrates successful spreading of the cold film over the downstream surface not only in the streamwise direction but also in the spanwise fashion. The force density increase has a significant influence on the cold flow attachment just downstream of the coolant hole (see Fig. 8b). The effectiveness is plotted in Fig. 9 against a nondimensional ratio of x/Md, where x is the downstream distance, M is the blowing ratio, and d is the circular pipe diameter. The computed centerline effectiveness results for the baseline case (with no actuation) compare reasonably with the experiment of Sinha et al. [15] and two other previously reported numerical results [29,30] as shown in Fig. 9a. We can see the centerline effectiveness decreases for the baseline case as the distance of downstream (x/d) increases due to the liftoff effect. The result predicted by our model is similar to two other numerical predictions [29,30]. In Fig. 9b, as the force density increases to the maximum, the centerline effectiveness increases by over 100% than the baseline case.

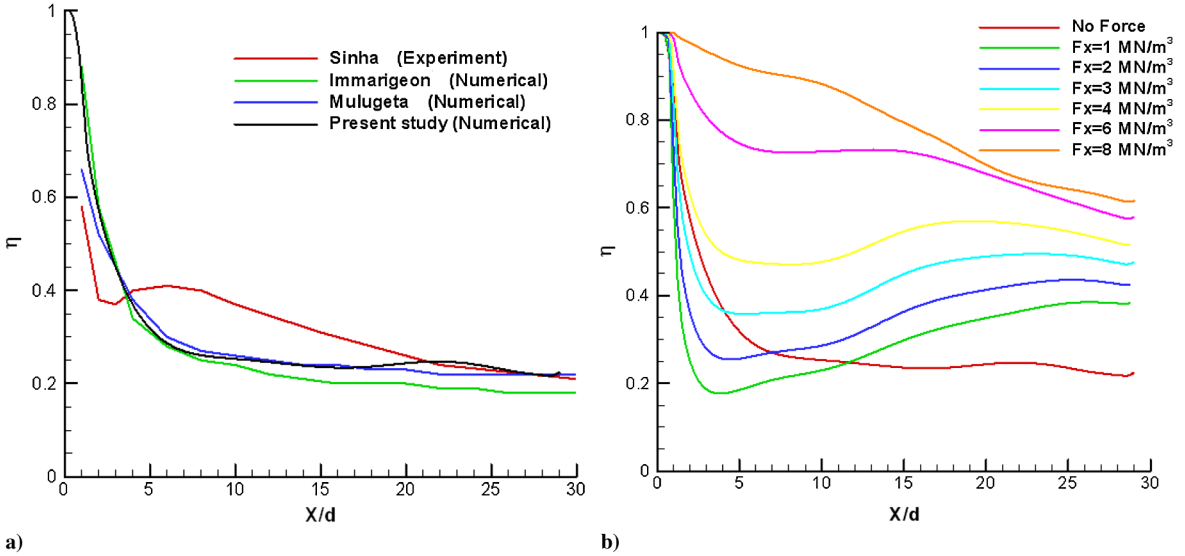

Fig. 9 Comparison of centerline effectiveness for a) the baseline case and b) different plasma force densities.

V. Conclusions

The contribution of this numerical work is to successfully apply first principles based plasma force to enhance film cooling effectiveness. We solved the plasma governing equations using a finite element based MIG flow code to predict the induced plasma force and used that body force in the Navier–Stokes equations employing a finite volume based commercial ANSYS Fluent software. Two problems were investigated using horseshoe shaped plasma actuators. For problem I, we tested three different cases with very low speed bulk (0.3 m/s) and coolant (0.42 m/s) flows to find a higher film cooling effectiveness on the work surface. Based on the temperature distribution, the electrode arrangement for an inward plasma force predicts better jet attachment to the work surface downstream of the coolant hole. The predicted force density of the horseshoe actuator in this case was $\sim kN/m^3$, which required a few watts of power for the surface area considered. In an actual gas turbine (blowing ratio ~ 1, problem II), a force density of MN/m^3 was required for an effective flow control. Such a high force density was deemed viable due to the recent development of microscale actuators. As we varied the electric force density from 0 (no force) to 8 MN/m^3, we found significant improvements for both streamwise and spanwise film cooling effectiveness in comparison to the baseline case. For the maximum force density, the improvement of centerline effectiveness was about 260% than the baseline case at a downstream location of $x = 10d$. The baseline case was in good agreement with reported experimental data and other numerical work. Simulation results indicate that plasma augmented flow control ideas may become more beneficial for energy budget management in film-cooling applications especially for cases with largely separated jets at higher blowing ratios.

Acknowledgments

This work was partially supported by the Air Force Office of Scientific Research Grants monitored by Douglas Smith. The authors also acknowledge partial support from the Florida Center for Advanced Aero-Propulsion for this research.

References

[1] Haven, B. A., and Kurosaka, M., "Kidney and Anti-Kidney Vortices in Crossflow Jets," *Journal of Fluid Mechanics*, Vol. 352, Dec. 1997, pp. 27–64. doi:10.1017/S0022112097007271

[2] Roy, S., "Numerical Investigation of the Blade Cooling Effect by Multiple Jets Issuing at an Angle," *Numerical Heat Transfer*, Vol. 38, No. 7, 2000, pp. 701–718. doi:10.1080/10407780050195652

[3] Walters, D. K., and Leylek, J. H., "A Detailed Analysis of Film Cooling Physics: Part I—Streamwise Injection with Cylindrical Holes," *Journal of Turbomachinery*, Vol. 122, No. 1, 2000, pp. 102–112. doi:10.1115/1.555433

[4] Hyams, D. G., and Leylek, J. H., "A Detailed Analysis of Film Cooling Physics: Part III—Streamwise Injection with Shaped Holes," *Journal of Turbomachinery*, Vol. 122, No. 1, 2000, pp. 122–132. doi:10.1115/1.555435

[5] Azzi, A., and Jubran, B. A., "Numerical Modeling of Film Cooling From Converging Slot-Hole," *International Journal of Heat and Mass Transfer*, Vol. 43, No. 4, 2007, pp. 381–388. doi:10.1007/s00231-006-0115-9

[6] Zhang, X. Y., and Hassan, I. G., "Film Cooling Effectiveness of an Advanced-Louver Cooling Scheme for Gas Turbine," *Journal of Thermophysics and Heat Transfer*, Vol. 20, No. 4, 2006, pp. 754–763. doi:10.2514/1.18898

[7] Na, S., and Shih, T. I. P., "Increasing Adiabatic Film-Cooling Effectiveness by Using an Upstream Ramp," *Journal of Heat Transfer*, Vol. 129, No. 4, 2007, pp. 464–471. doi:10.1115/1.2709965

[8] Garg, V. K., "Heat Transfer on a Film-Cooled Rotating Blade," *International Journal of Heat and Fluid Flow*, Vol. 21, No. 2, 2000, pp. 134–145. doi:10.1016/S0142-727X(99)00072-7

[9] Heidmann, J. D., Rigby, D. L., and Ameri, A. A., "A Three-Dimensional Coupled Internal/External Simulation of a Film-Cooled Turbine Vane," *Journal of Turbomachinery*, Vol. 122, No. 2, 2000, pp. 348–359. doi:10.1115/1.555450

[10] Wilcox, D. C., "Re-Assessment of the Scale-Determining Equation for Advanced Turbulence Models," *AIAA Journal*, Vol. 26, No. 11, 1988, pp. 1299–1310. doi:10.2514/3.10041

[11] Zhong, F., and Brown, G. L., "A 3-Dimensional, Coupled, DNS, Heat Transfer Model and Solution for Multi-Hole Cooling," *International Journal of Heat and Mass Transfer*, Vol. 50, Nos. 7–8, 2007, pp. 1328–1343. doi:10.1016/j.ijheatmasstransfer.2006.09.017

[12] Kapadia, S., Roy, S., and Heidmann, J. D., "First Hybrid Turbulence Modeling for Turbine Blade Cooling," *Journal of Thermophysics and Heat Transfer*, Vol. 18, No. 1, 2004, pp. 154–156. doi:10.2514/1.2824

[13] Martini, P., Schulz, A., and Bauer, H. T., "Detached Eddy Simulation of Film Cooling Performance on the Trailing Edge Cutback of Gas Turbine Airfoils," *Journal of Turbomachinery*, Vol. 128, No. 2, 2006, pp. 292–299. doi:10.1115/1.2137739

[14] Kim, S. I., and Hassan, I. G., "Unsteady Heat Transfer Analysis of a Film Cooling Flow," *46th AIAA Aerospace Sciences Meeting and Exhibit*, American Institute of Aeronautics and Astronautics Inc., Reston, VA, AIAA Paper 2008-1287, Jan. 2008, pp. 1–12.

[15] Sinha, A. K., Bogard, D. G., and Crawford, M. E., "Film-Cooling Effectiveness Downstream of a Single Row of Holes with Variable Density Ratio," *Journal of Turbomachinery*, Vol. 113, No. 3, 1991, pp. 442–449. doi:10.1115/1.2927894

[16] Bell, C. M., Hamakawa, H., and Ligrani, P. M., "Film Cooling from Shaped Holes," *Journal of Heat Transfer*, Vol. 122, No. 2, 2000, pp. 224–232. doi:10.1115/1.521484

[17] Bunker, R. S., "A Review of Shaped Hole Turbine Film-Cooling Technology," *Journal of Heat Transfer*, Vol. 127, No. 4, 2005, pp. 441–453. doi:10.1115/1.1860562

[18] Ekkad, S. V., Ou, S., and Rivir, R. B., "Effect of Jet Pulsation and Duty Cycle on Film Cooling from a Single Jet on a Leading Edge Model," *Journal of Turbomachinery*, Vol. 128, No. 3, 2006, pp. 564–571. doi:10.1115/1.2185122

[19] Bogard, D. G., and Thole, K. A., "Gas Turbine Film Cooling," *Journal of Propulsion and Power*, Vol. 22, No. 2, 2006, pp. 249–270. doi:10.2514/1.18034

[20] Moreau, E., "Airflow Control by Non-Thermal Plasma Actuators," *Journal of Physics D: Applied Physics*, Vol. 40, No. 3, 2007, pp. 605–636. doi:10.1088/0022-3727/40/3/S01

[21] Corke, T. C., Enloe, C. L., and Wilkinson, S. P., "Dielectric Barrier Discharge Plasma Actuators for Flow Control," *Annual Review of Fluid Mechanics*, Vol. 42, No. 1, 2010, pp. 505–529. doi:10.1146/annurev-fluid-121108-145550

[22] Roy, S., and Wang, C. C., "Plasma Actuated Heat Transfer," *Applied Physics Letters*, Vol. 92, No. 23, 2008, pp. 231501–231501-3. doi:10.1063/1.2938886

[23] Wang, C. C., and Roy, S., "Electrodynamic Enhancement of Film Cooling of Turbine Blades," *Journal of Applied Physics*, Vol. 104, 2008, Paper 073305. doi:10.1063/1.2990074

[24] Gregory, J. W., Enloe, C. L., Font, G. I., and McLaughlin, T. E., "Force Production Mechanisms of a Dielectric-Barrier Discharge Plasma Actuator," *45th AIAA Aerospace Sciences Meeting and Exhibit*, American Institute of Aeronautics and Astronautics Inc., Reston, VA, AIAA Paper 2007-185, Jan. 2007, pp. 2191–2203.

[25] Kumar, H., and Roy, S., "Multidimensional Hydrodynamic Plasma-Wall Model for Collisional Plasma Discharges with and Without Magnetic Field Effects," *Physics of Plasmas*, Vol. 12, No. 9, 2005, pp. 093508–093508-10. doi:10.1063/1.2044747

[26] Surzhikov, S. T., and Shang, J. S., "Two-Component Plasma Model for Two-Dimensional Glow Discharge in Magnetic Field," *Journal of Computational Physics*, Vol. 199, No. 2, 2004, pp. 437–464. doi:10.1016/j.jcp.2004.02.019

[27] Hagelaar, G. J. M., and Pitchford, L. C., "Solving the Boltzmann Equation to Obtain Electron Transport Coefficients and Rate Coefficients for Fluid Models," *Plasma Sources Science and Technology*, Vol. 14, No. 4, 2005, pp. 722–733. doi:10.1088/0963-0252/14/4/011

[28] Zhang, X. Z., and Hassan, I., "Film Cooling Effectiveness of an Advanced-Louver Cooling Scheme for Gas Turbine," *Journal of Thermophysics and Heat Transfer*, Vol. 20, No. 4, 2006, pp. 754–764. doi:10.2514/1.18898

[29] Immarigeon, A. A., "Advanced Impingement/Film-Cooling Schemes for High-Temperature Gas Turbines: Numerical Study," M.S. Thesis, Dept. of Mechanical and Industrial Engineering, Concordia Univ., Montreal, 2004.

[30] Berhe, M. K., and Patankar, S. V., "A Numerical Study of Discrete-Hole Film Cooling," *American Society of Mechanical Engineers*, Paper 96-WA/HT-8, 1996.

[31] Wilson, C. G., Gianchandani, Y. B., Arslanbekov, R. R., Kolobov, V., and Wendt, A. E., "Profiling and Modeling of DC Nitrogen Microplasmas," *Journal of Applied Physics*, Vol. 94, No. 5, 2003, pp. 2845–2851. doi:10.1063/1.1595143

[32] Wilson, C. G., and Gianchandani, Y. B., "Selective Deposition of Silicon at Room Temperature Using DC Microplasmas," *IEEE Transactions on Plasma Science*, Vol. 35, No. 3, 2007, pp. 573–577. doi:10.1109/TPS.2007.897412

[33] Zito, J., Durscher, R., Soni, J., Roy, S., and Arnold, D., "Flow and Force Inducement Using Micro Size Dielectric Barrier Discharge Actuators," *Applied Physics Letters*, Vol. 100, No. 19, 2012, Paper 193502. doi:10.1063/1.4712068

[34] Roy, S., and Wang, C. C., "Bulk Flow Modification with Horseshoe and Serpentine Plasma Actuators," *Journal of Physics D: Applied Physics*, Vol. 42, No. 3, 2009, Paper 032004. doi:10.1088/0022-3727/42/3/032004

[35] Rizzetta, D. P., and Visbal, M. R., "Large-Eddy Simulation of Plasma-Based Turbulent Boundary-Layer Separation Control," *AIAA Journal*, Vol. 48, No. 12, 2010, pp. 2793–2810. doi:10.2514/1.J050014

[36] Durscher, R., and Roy, S., "Three-Dimensional Flow Measurements Induced from Serpentine Plasma Actuators in Quiescent Air," *Journal of Physics D: Applied Physics*, Vol. 45, No. 3, 2012, Paper 035202. doi:10.1088/0022-3727/45/3/035202